High temperature magnetism and microstructure of ferromagnetic alloy $Si_{1-x}Mn_x$

2017 J. Phys.: Condens. Matter 29 055802

(http://iopscience.iop.org/0953-8984/29/5/055802)

IOP Publishing
Journal of Physics: Condensed Matter
J. Phys.: Condens. Matter **29** (2017) 055802 (10pp)
doi:10.1088/1361-648X/29/5/055802

High temperature magnetism and microstructure of ferromagnetic alloy $Si_{1-x}Mn_x$

B A Aronzon[1,2], **A B Davydov**[2], **A L Vasiliev**[1], **N S Perov**[3], **O A Novodvorsky**[4], **L S Parshina**[4], **M Yu Presniakov**[1] **and E Lahderanta**[5]

[1] NRC 'Kurchatov institute', Moscow, Russia
[2] Lebedev Physical Institute RAS, Moscow, Russia
[3] M.V. Lomonosov MSU, Moscow, Russia
[4] Institute of Laser and Information Technologies RAS, Shatura, Russia
[5] Lappeenranta University of Technology, Lappeenranta, Finland

E-mail: aronzon@mail.ru

Received 17 August 2016, revised 13 October 2016
Accepted for publication 18 October 2016
Published 2 December 2016

Abstract

The results of a detailed study of magnetic properties and of the microstructure of SiMn films with a small deviation from stoichiometry are presented. The aim was to reveal the origin of the high temperature ferromagnetic ordering in such compounds. Unlike SiMn single crystals with the Curie temperature ~30 K, considered $Si_{1-x}Mn_x$ compounds with $x = 0.5 + \Delta x$ and Δx in the range of 0.01–0.02 demonstrate a ferromagnetic state above room temperature. Such a ferromagnetic state can be explained by the existence of highly defective B20 SiMn nanocrystallites. These defects are Si vacancies, which are suggested to possess magnetic moments. The nanocrystallites interact with each other through paramagnons (magnetic fluctuations) inside a weakly magnetic manganese silicide matrix giving rise to a long range ferromagnetic percolation cluster. The studied structures with a higher value of $\Delta x \approx 0.05$ contained three different magnetic phases: (a)—the low temperature ferromagnetic phase related to SiMn; (b)—the above mentioned high temperature phase with Curie temperature in the range of 200–300 K depending on the growth history and (c)—superparamagnetic phase formed by separated noninteracting SiMn nanocrystallites.

Keywords: high temperature magnetic semiconductor, manganese silicide, microstructure, ferromagnetic ordering, paramagnons

(Some figures may appear in colour only in the online journal)

1. Introduction

Currently the most widely studied dilute magnetic semiconductor (DMS) materials are those based on III–V semiconductors doped by Mn [1–3]. Ferromagnetic (FM) ordering in this case occurred due to carrier-induced indirect exchange between Mn atoms accompanied by the spin polarization of holes, which can reach 80% [4]. However, the highest Curie temperature T_C achieved for these materials does not exceed 200 K [5], while the desired one is $T_C > 300$ K. Thus the search for new spintronic materials has to be continued.

Si-based DMSs are very attractive for the developing of spintronics elements, because they can be easily integrated into modern microelectronic technology [6]. One of the first attempts to produce such materials was made by the implantation of Mn ions into Si crystal [7]. This work attracted significant attention due to the observation of a FM state with a high Curie temperature $T_C > 400$ K, although these materials contain a relatively low (0.1–0.8 at.%) amount of Mn dopants. Later a high temperature FM state was observed in Si also after implantation of nonmagnetic ions (Ar, Si) or irradiation by neutrons. The origin of these phenomena remained

Table 1. $Si_{1-x}Mn_x$ film parameters.

Sample number	Growth temp Tg (°C)	XPS estimated Mn content, x	Film thickness.d, (nm)	Film resistivity ρ, (m $\Omega\cdot$ cm), at 300 K
1	340	≈0.52	70	0.18
2	340	0.51	57	0.25
3	340	0.55	60	0.44
4	340	0.55	70	0.33

mysterious. They were called 'puzzled ferromagnetism' and some authors argued that high-temperature FM in Si-based DMSs originated due to paramagnetic defects [8, 9]. It was found that the magnetization in such structures was very weak and was not detected by transport measurements, in particular, by the anomalous Hall effect, which could be used for the detection of carriers spin-polarization. The low-temperature ferromagnetism, with a saturation moment of $\approx 0.21\mu_B$ per Mn atom, was observed in a number of studies [10–13]. However, weak magnetization and the absence of carrier spin-polarization make these materials inappropriate for spintronic devices.

Recently a ferromagnetic state at room temperature was observed in $Si_{1-x}Mn_x$ alloys with high Mn content [14]. This was detected by direct magnetic measurements and by the observation of anomalous Hall effect (AHE), which indicated the existence of the carrier spin polarization [14–17]. These structures were grown by the droplet free pulsed laser deposition (PLD) method with different schemes of separation [15, 17, 18]. They demonstrated Curie temperature T_C above 300 K. Combined simultaneous deposition of Mn and Si yield in the growth of manganese silicide Mn_nSi_m films. Films with Mn content close to 35 at% were formed in [14]. The composition corresponds to $m/n \approx 1.86$ with the crystal structure close to that of Mn_4Si_7, which is equivalent to $MnSi_{1.75}$. The magnetic moments were believed to be related to the Mn:Si non-stoichiometry and originated from the angstrom-sized magnetic defects (single Mn ions or molecular complexes containing Mn), denoted by the symbol Mn_d and it was assumed that $MnSi_{1.86} = (MnSi_{1.75})_{1-\lambda}(Mn_d)_\lambda$ [14]. The Mn_4Si_7 is a weak helicoidal itinerant ferromagnet with $T_C < 50$ K. The interpretation of the results was based on the model [19], which implied that magnetic properties appear due to the above mentioned structural defects, which reveal the magnetic moment. The exchange between magnetic moments was suggested to occur via spin fluctuations (paramagnons) inside the matrix and leads to a strong increase in T_C. However, there is a number of other silicides with m/n ranging from 1.70–1.75 (for example, Mn_4Si_7, $Mn_{11}Si_{19}$, $Mn_{15}Si_{26}$, $Mn_{26}Si_{45}$, $Mn_{27}Si_{47}$) [20]. Thus, the compound with Mn content ≈0.35 could contain a mixture of these weak ferromagnet silicides.

For the sake of simplicity it was suggested to study high temperature ferromagnetism in compounds with m/n close to 1, which is far enough from the above mentioned compositions and from the silicides with low Si content (Mn_5Si_3, Mn_5Si_2). In addition it should be mentioned that the MnSi nowadays is of great interest due to its unique properties [21–26].

$Si_{1-x}Mn_x$ films with $x \approx 0.5$, which were formed by the droplet free PLD technology, also demonstrated high temperature ferromagnetic state accompanied with anomalous Hall effect [15–17]. Again, to explain the room temperature ferromagnetism the same model [19] was used: the high temperature ferromagnetism is related to local ferromagnetic moments originating from the deviation of the stoichiometry; the interaction between them occurs through paramagnons. The reason for such a suggestion is that MnSi is a weak itinerant ferromagnet and at $T > T_C \approx 30$ K there is an essential concentration of spin fluctuations [19].

The Mn silicides belong to the Berthollide type of compounds, a solid compound with slight variations in chemical composition depending on the prehistory [21]. The properties of Berthollides are very sensitive to the fabrication technology used and this fully applies to MnSi samples with small deviation from stoichiometry. For example, high temperature ferromagnetism was not found in the samples grown by MBE [27], implantation or sputtering [6]. The variation of the PLD technique ('shadow' technique) could result in a high temperature ferromagnetic $Si_{1-x}Mn_x$ located at the film/substrate interface [17], but not in the bulk of the film and that differs from the data obtained for samples in the present paper.

To reveal the origin of the high temperature ferromagnetism in $Si_{1-x}Mn_x$ compounds, one needs a detailed knowledge of the sample structure. The aim of this paper is to present magnetic properties of the $Si_{1-x}Mn_x$ films with x in the range of ≈ 0.5–0.55 accompanied with detailed scanning/transmission electron microscopy (SEM/TEM) studies of the structure and to elucidate the origin of the ferromagnetic state in this material. In this context, the goal is to clarify the microscopic nature of the long-range high-temperature ferromagnetic state in the system.

2. Samples and methods

$Si_{1-x}Mn_x$ films with the thickness (d) in the range from 57 nm to 70 nm and composition close to the manganese monosilicide SiMn ($x = 0.5$) were grown by the droplet-free PLD method by 248 nm excimer laser radiation on (0 0 0 1) α-Al_2O_3 substrates with the time-of-flight separation system. This technology has been described in [28]. The energy spectrum of the particles was controlled by focusing the laser beam on the target during growth. The pressure was 10^{-7} Torr and the substrate temperature T_g was stabilized at 340 °C. The film composition was estimated by XPS after ion etching of the surface during 60 s to remove a 5–10 nm surface layer.

The film composition, thickness and electrical resistivity for four studied samples are listed in table 1. For simplicity we will use the averaged XPS data for the sample composition identification. The sample resistivity at room temperature

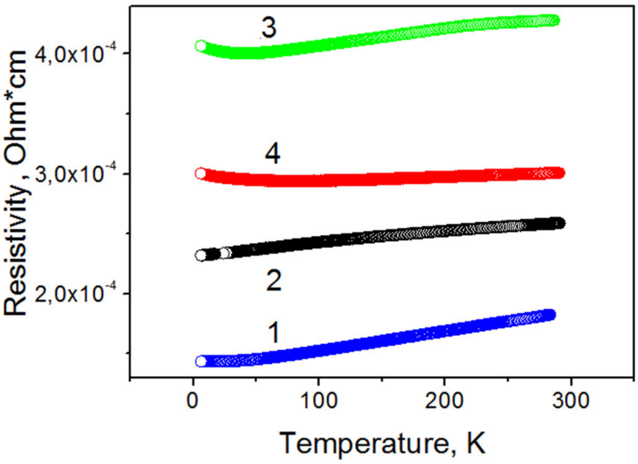

Figure 1. Temperature dependence of the $Si_{1-x}Mn_x/Al_2O_3$ samples resistivity. For each sample its number is shown near the curve.

was in the range of 0.18–0.44 · mΩ cm (table 1), which is typical for semimetals or heavily doped semiconductors [29]. All samples were of p-type with carrier concentration p being about $p \approx 2 \times 10^{21}$ cm^{-3}. Resistivity ρ of the samples 1 and 2 demonstrated metallic behavior $\mathrm{d}\rho/\mathrm{d}T > 0$, while for the samples 3 and 4 at low temperatures (less than 60 K) the resistivity rises with temperature decrease $\mathrm{d}\rho/\mathrm{dT} < 0$ (figure 1). In accordance with that all samples were divided into two groups. Samples 1 and 2 belong to the 'a-type' group while 3 and 4 to the 'b-type' one. The difference between these two groups is the value of the deviation from stoichiometry Δx which is higher for the 'b-type' $\Delta x \approx 0.05$ and smaller for the 'a-type' group $\Delta x \approx 0.01 - 0.02$ (table 1). The disorder in the 'b-type' group of samples is stronger as it will be demonstrated below by the results of the SEM/TEM study. This results in higher resistivity values and insulator like conductivity for the 'b-type' samples, while for the 'a-type' group the resistivity is smaller and shows metallic behavior $\mathrm{d}\rho/\mathrm{d}T > 0$. It leads also to quite different magnetic properties for these two groups of samples as it will be discussed in the following section of the paper.

The samples cross-section for the SEM/TEM was prepared by focus ion beam (FIB) milling procedure in a Helios (FEI, OR, US) scanning electron microscope (SEM)/FIB dual beam system equipped with C and Pt contain gas injectors and a micromanipulator (Omniprobe, TX, US). A 2 μm Pt layer was deposited on the surface of the sample prior to the cross-sections preparation by FIB milling procedure. Sections approximately 8×5 μm^2 in size and 2 μm thick were cut by 30 kV Ga^+ ions, removed from the sample and then attached to the Omniprobe semiring (Omniprobe, TX, US). Final thinning was performed with 5 kV Ga^+ ions followed by cleaning by 2 keV Ga^+ ions to the electron transparency. All specimens were studied in a transmission/scanning electron microscope (TEM/STEM) Titan 80–300 (FEI, OR, US) equipped with a spherical aberration (Cs) corrector (electron probe corrector), a high angle annular dark field (HAADF) detector, an atmospheric thin-window energy dispersive x-ray (EDX) spectrometer (Phoenix System, EDAX, NJ, USA) and post-column Gatan energy filter (GIF), (Gatan,CA, US). The TEM was operated at 300 kV. Digital micrograph (Gatan, Pleasanton, CA, US) and TIA (FEI, OR, US) software was used for image analysis. P.Stadelmann's JEMS software [30] was used for diffraction patterns and image simulation.

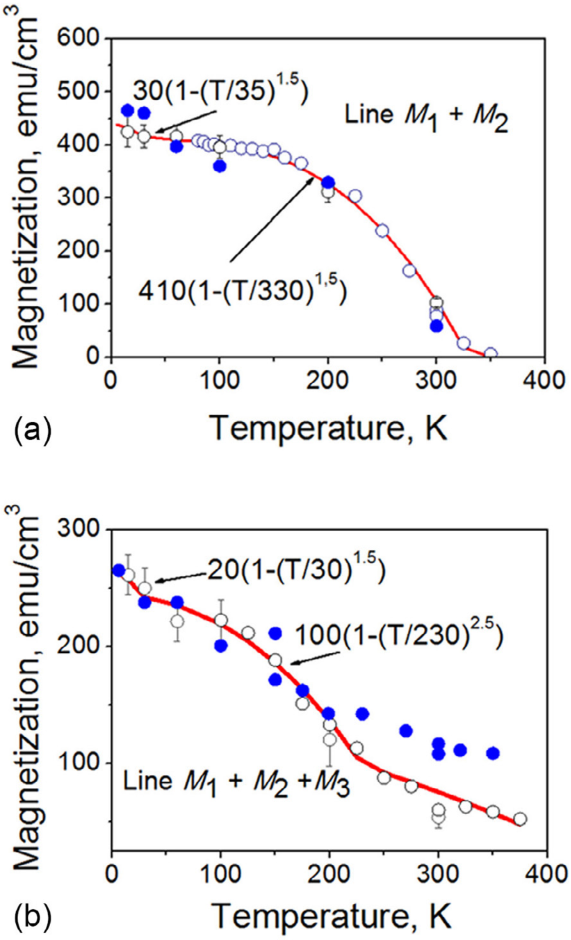

Figure 2. (a) Temperature dependence of the saturation magnetization (M_s) of $Si_{1-x}Mn_x/Al_2O_3$ samples 1 (white circles) and 2 (dark circles). Sample 2 data has been multiplied by the factor of 2.8. The curve is fitting with equation (3). Fitting parameters are shown near the curve. (b) Temperature dependence of the saturation magnetization (M_s) of the $Si_{1-x}Mn_x/Al_2O_3$ samples 3 (white circles) and 4 (dark circles). Sample 4 data multiplied by the factor of 3. The curve is fitting with equation (3). Fitting parameters are shown near the curve.

3. Magnetometry results

Temperature dependence of the saturation magnetization M_s in a wide temperature range as well as the measurements of ZFC, FC and thermo-magnetoremanence curves indicated that the films contained three different magnetic phases (low temperature ferromagnetic, high temperature ferromagnetic and superparamagnetic). The $M_s(T)$ curves for four studied samples are presented in figure 2. As it was mentioned above the samples can be divided into two groups designated as 'a-type' and 'b-type' and their magnetization curves are presented in figures 2(a) and (b), respectively. The magnetization curves $M_s(T)$ (figures 2(a) and (b)) demonstrate that for each

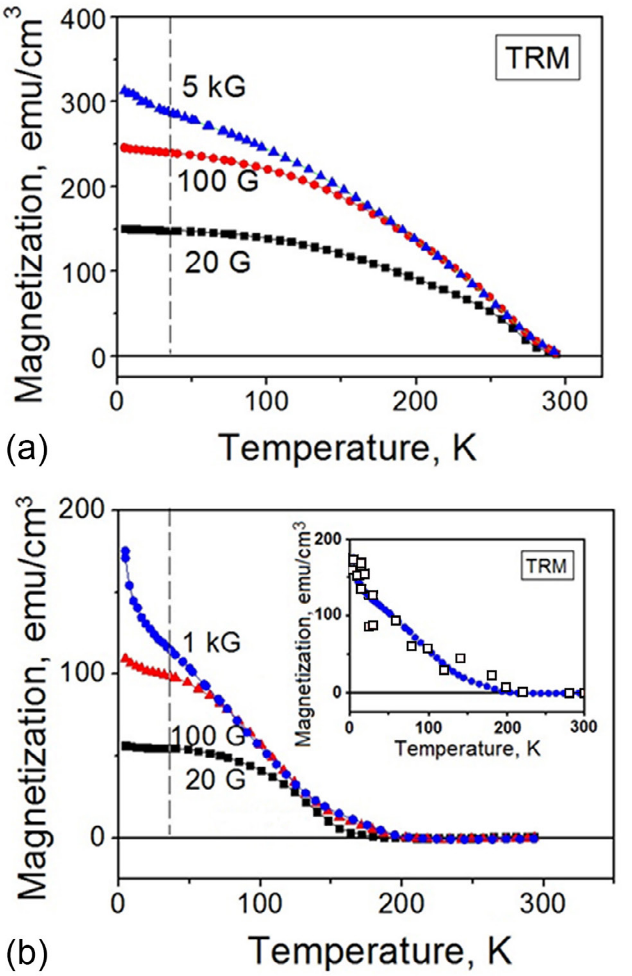

Figure 3. (a) The temperature dependence of the remanent magnetization (TermoRemanence Magnetization TRM) for sample 1 after cooling in the field shown near the curves. Dashed line corresponds to 35 K, that is the end of the first temperature range. It is seen that the slope of the 5 kG curve changes near this temperature. (b) The temperature dependence of the remanent magnetization (termoremanence magnetization TRM) for sample 3 after cooling in the field shown near the curves. The insert shows the comparison of TRM curves for samples 3 (filled circle) and 4 (open square) measured after switched off 1 kG. The data for sample 4 is multiplied by a factor of 3. The dashed line corresponds to 30 K, that is the end of the first temperature range. It is seen that the slope of the 1 kG curve changes near this temperature.

sample there are 3 temperature ranges with different behavior. One can see that at low temperatures (below 30–35 K) the $M_s(T)$ curves for all samples demonstrate the tendency to bend to upper values. That is a hint for a stronger M_s temperature dependence in this temperature range. More clearly it is seen for the temperature dependence of the remanent magnetization after cooling at high enough fields presented in figures 3(a) and (b). So the first temperature range is below 30–35 K for all the samples. For the samples 3 and 4 the second temperature range is between 40 and 230 K (for the sample 4, dark points between 35 and 200 K) and the third range is above 230 K (200 K for dark points) (figure 2(b)). For the samples 1 and 2 the second range is much wider (figure 2(a)) and ranges above room temperature. Below 35 K we observed an abrupt slope

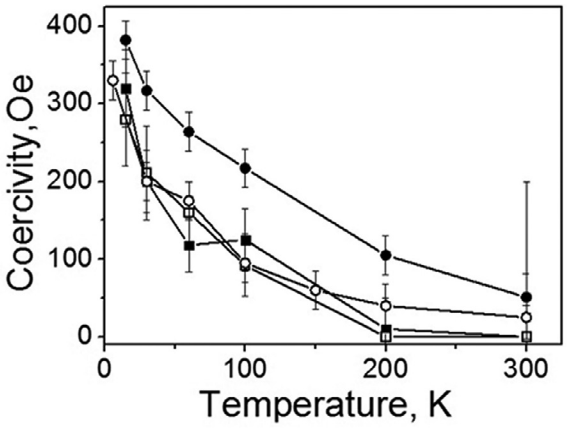

Figure 4. Coercivity versus temperature for samples: 1 (black circle); 2 (white circle); 3 (black square); 4 (white square).

of $M_s(T)$ for all samples (figure 3), while the third range for samples 1 and 2 is very narrow.

To describe the observed $M_s(T)$ behavior we have used the Brillouin function in the following form as it is usually done for diluted magnetic semiconductors

$$M_s\left({}^{T}\!/_{T_C}\right) \approx 1-\left({}^{T}\!/_{T_C}\right)^n, \tag{1}$$

which is valid for RKKY/Zener mechanism, where the exchange integral does not depend on the temperature and $n \approx 2$ for GaMnAs [31]. For the exchange mechanism between magnetic moments via spin fluctuations (paramagnons), suggested for $Si_{1-x}Mn_x$ structures [19], the exchange integral J_{sf} is temperature dependent and the $M_s(T)$ dependence could be described by the expression [14]:

$$M_s(T) \approx M_s(0)\{1-[T(T-T_C^0)/T_C(T_C-T_C^0)]^n\},$$

where T_C^0 the Curie temperature of the host matrix. However, in our case the Curie temperature of the structure is $T_C \gg T_C^0$, and a simplified expression (1) could be used. According to three temperature ranges with various dependences observed in our measurements, a three-term equation should be used to fit the $M_s(T)$ curve

$$M_s(T) \ = M_{s1}(T)+M_{s2}(T)+M_{s3}(T). \tag{2}$$

It is reasonable to assume that three terms in equation (2) are related to three different magnetic phases, which contribute to the sample magnetization. $M_{si}(T)$ is saturation magnetization for *i*-phase. To describe the temperature dependence of magnetization, $M_{s1}(T)$ and $M_{s2}(T)$ in equation (2) could be approximated by a simplified function (1) $M_{si} = M_{si}(0)$ $[1-(T/T_{Ci})^{ni}]$. Here $M_{si}(0)$ is the saturation magnetization at zero temperature, T_{Ci}—Curie temperature and n_i—the exponent for each phase. The third magnetic phase, related to the third temperature range, is observed mainly above room temperatures and mainly in the samples of the 'b-type'. $M_{s3}(T)$ also can be fitted by the same simplified equation, as the first and the second phases. However, most probably it is related to the contribution of the superparamagnetic inclusions (see below). This is in agreement with zero values of M_r and coercivity H_c (shown in figures 3 and 4 respectively) for 'b-type' samples 4 and 3 in the corresponding temperature range while M_s is nonzero. So, finally for a three-term equation we have:

$$M_s(T) = M_{s1}(0)[1-(T/T_{C1})^{n1}] + M_{s2}(0)[1-(T/T_{C2})^{n2}] + M_{s3}(T), \quad (3)$$

where $M_{s3}(T)$ is the temperature dependence of the magnetization of the superparamagnetic phase. $M_s(T)$ experimental data are very well fitted using this equation (see figure 2). Each phase contributes to the $M_s(T)$ curve in its specific temperature range. Figures 2(a) and (b) demonstrate that the $M_s(T)$ dependences for the samples from the same group are similar while these curves for samples from various groups, namely 'a' and 'b', are different: For the group 'b' the second temperature range is shorter while the third range is wider.

M_s data for the samples 2 and 4 presented in figures 2(a) and (b) were multiplied by the factors 2.8 and 3.0, respectively, to make the similarity to the samples 1 and 3 more obvious and to mark out the temperature dependence of the $M_s(T)$ for the comparison of their behavior for different samples. The magnetic moments per Mn atom, μ, at saturation ranges for 'a-type' samples from 1.4 to 0.6μ_B/Mn at 30 K and from 0.3 to 0.1μ_B/Mn at 300 K, while for 'b-type' samples it is between 0.7–0.25μ_B/Mn at 30 K and 0.15–0.05μ_B/Mn at 300 K. The difference of M_s values for various samples is due to changes of technological parameters, sometimes their lack of stability resulted in the variation of composition. The variation and the nonhomogeneity of the composition of the samples grown by the PLD will be considered on the basis of SEM/TEM results. As we mentioned above, one of the goals was to distinguish the high temperature phase in order to obtain uniform compound in future.

We assume that the first phase, which exists in all samples and has approximately the same fitting parameters is related to the SiMn. This assumption is supported by the value of its Curie temperature $T_{C1} \approx 35$ K and 30 K (for *a* and *b* types of samples), which is close to T_C for SiMn. The contribution of this phase is supported by the curves presented in figures 3(a) and (b), which demonstrate the remanent magnetization M_r (thermoremanent magnetization—TRM) versus temperature for samples 1 (figure 3(a)) and 3 (figure 3(b)). The inset of figure 3(b) demonstrates the similarity of the temperature dependencies of magnetic properties for the samples 3 and 4 (The data for 4 sample also multiplied by factor of 3 as it was done for the curves in figure 2). Here the existence of the first low-temperature phase is much more visible. Figure 3 demonstrates that with the increasing of temperature the M_r of the low-temperature phase decreases much faster than the high-temperature phases resulting in distinguishability of this phase (it is seen more clearly after cooling in high fields).

As mentioned above, due to this technological process the contribution of different phases could vary from sample to sample. For samples 1 and 2 the contribution of the first, low-temperature phase, is weaker than that for the samples 4 and 3. The similarity of the first phase fitting parameters for all samples is in agreement with the assumption that this phase is MnSi of B20 structure [24], which demonstrates ferromagnetic behavior at temperatures below 40 K. The remanent magnetization M_{r1} related to this low temperature phase relaxes fast with temperature (see figure 3) and also with time after switching off the magnetic field as it was observed during the magnetization measurements (not shown here). According to time relaxation of the $M_{r,}$ its low temperature value is smaller than that of M_s, the M_r low temperature value is smaller than that of M_s, because M_r diminished with time due to $\partial M_r/\partial t$ during delay between the two sets of measurements.

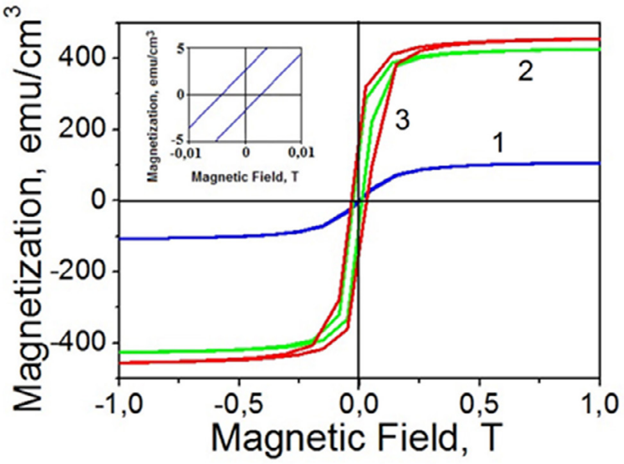

Figure 5. Magnetization versus magnetic field at different temperatures: 300 K (curve 1), 100 K (curve 2) and 15 K (curve 3) for the sample 1. Inset: zoom of the 300 K curve.

As it was mentioned above, we assume that the third magnetic phase $M_{s3}(T)$ observed above room temperature mainly in samples of the 'b-type' is superparamagnetic one. Unlike 'b-type' samples, for the 'a-type' samples 1 and 2 the $M_3(T)$ contribution can be neglected because of its small impact. The assumption of superparamagnetic nature for the third phase is supported by zero values of M_r and coercivity H_c for 'b-type' samples in the temperature range, where the third phase is active, $T > 200$ K (see figures 3 and 4). While for 'a-type' samples with negligible third phase contribution $H_c \neq 0$ and the hysteresis behavior is observable in the whole temperature range (see figures 4 and 5). The zero field and field cooling (ZFC and FC) curves (figure 6) demonstrate behavior of magnetization typical for superparamagnetic materials that also confirms the magnetic nanoparticles existence in these samples.

The second phase is the most interesting and promising for applications. It shows ferromagnetic behavior above room temperature. In 'a-type' samples it is more pronounced and seen in a wider temperature range. The room temperature ferromagnetic ordering for samples 1 and 2 is unambiguously demonstrated by the $M_s(T)$ dependence presented in figure 2(a), and by the hysteresis behavior of the $M(B)$ curves shown in figure 5. Figure 5 presents the $M(B)$ curves at temperatures 300, 100 and 15 K. The hysteresis is observed even at room temperature (see inset of figure 5), proving the ferromagnetic state of this phase. In figures 2 and 5(a) it is seen that the profile of the $M(B)$ dependence hardly changes up to 100 K keeping approximately the same value for M_{s2}, while noticeable changes occur only above 200 K. It is found that the ferromagnetic ordering in the samples 1 and 2 still exists up to the

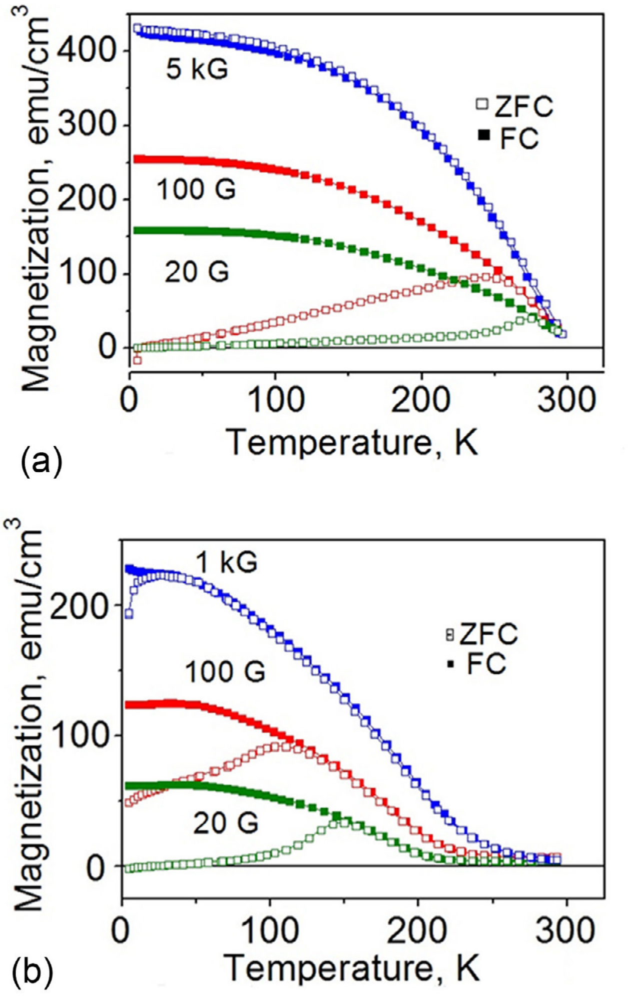

Figure 6. (a) ZFC (open squares) and FC (filled squares) magnetization of sample 1; respective values of the magnetic field are indicated near the curves. (b) ZFC (open squares) and FC (filled squares) magnetization of sample 3; respective values of the magnetic field are indicated near the curves.

room temperature and H_c value exceeds the error (figure 4). Fitting of $M_s(T)$ for this phase gives the values $M_{s2}(0) = 410$ emu cm^{-3} and $T_{C2} \approx 330$ K for the Curie temperature. These values and the high temperature ferromagnetic ordering are supported by the results of anomalous Hall effect measurements [16, 17]. Similar results for the second phase including anomalous Hall effect were now obtained for the samples 3 and 4 of ‘b-type’, but with smaller Curie temperature value $T_{C2} \approx 230$ K and $M_{s2}(0) = 100$ emu cm^{-3} obtained from the fitting parameters (figure 2(b)).

4. Results of TEM studies

To understand the nature of the high-temperature magnetization one needs detailed knowledge of the structure on atomic scale. Low-magnification bright field (BF) TEM cross-section image of Mn_xSi_{1-x} film on (0001)α-Al_2O_3 substrate (sample 2 of ‘a-type’) is shown in figure 7(a). The interface looks sharp and smooth. The results of energy-dispersive x-ray spectroscopy (EDS) line scan are presented in figure 7(b). The Mn in the middle of Mn_xSi_{1-x} film is slightly depleted, which is seen as the brighter band in figure 7(a). This was formed due to the decrease of Mn sector in the composite Mn-Si target, which was then recovered. The film exhibited columnar morphology, clearly visible in figure 8.

The composition along the sample thickness is not homogeneous. The film includes a surface layer and the Mn_xSi_{1-x}/(0 0 0 1)α-Al_2O_3 interface, where the sample composition is different. The composition in the main, medium part of the film volume is close to the XPS data obtained after 10 nm surface layer removing by etching and x varies between 0.51–052.

High Resolution TEM (HRTEM) study (figure 9) revealed the presence of an intermediate layer at the Mn_xSi_{1-x}/(0 0 0 1)α-Al_2O_3 interface with the thickness of 0.7–0.8 nm, marked by an arrow. The intermediate layer has bright contrast and clear crystalline structure: the image demonstrate the crystal planes with the period of 0.19 nm. That could be oxide layer, probably MnO_x, or silicate. Similar intermediate layer has not been observed in Si/α-Al_2O_3 in the previous studies summarized in the review by Aindow [32]. Thus, we propose that the layer is not crystalline SiO_x.

In the main, medium part of the film volume the nanocrystallites (nanocrystalline particles) with high density of structural defects are visible in the HR TEM images (see, for example, figure 9). The nanocrystalline particle size was of 2–5 nm (see figure 9). Figure 10 presents a single nanocrystalline particle (see figures 10(a) and (c)) to demonstrate its B20 crystal structure (figures 10(b) and (d)). As it is seen in figure 9 these nanocrystallites (nanocrystalline particles) are gathered in vertical layers and form polycrystalline columns separated by vertical amorphous layers. The fast Fourier transformed (FFT) from the film, presented in the inset of figure 9, indicated that the film adopted random polycrystalline structure without traces of texture. The radius of the circle on FFT image corresponds to interplanar distance of 0.21 nm. This is close to the most intense reflection 210 of MnSi with B20 crystal structure (Space group $P2_13$) with $d = 0.2035$ nm [33]. As the next step we carefully inspected the HR TEM images and performed FFT analysis of several areas, and the results are shown in figures 10(a) and (c). The maxima in FFT spectra and angles between them are also very close to B20 MnSi crystal structure in [2 1 4] zone axis, (reflections 120 and 121 are arrowed in figure 10(b)) and [2 1 3] zone axis (reflections 120 and 111 are arrowed in figure 10(d)) respectively. The filtered images of the grains, from which the FFT spectra were obtained, are shown in figures 10(b) and (d), respectively. However, we did not find periodicity $d_{110} = 0.322$ nm on the HRTEM images. That could be due to very high density of defects in the $Si_{1-x}Mn_x$ samples.

The cross-sectional HAADF STEM image of ‘b-type’ Mn_xSi_{1-x} film on (0 0 0 1)α-Al_2O_3 substrate is shown in figure 11. The film exhibited polycrystalline microstructure with large amorphous fraction. Sample 4, similarly to the samples of ‘a-type’ contains layers at the surface and near the interface with a composition different from that of the medium part. The composition of the medium part is in agreement with XPS results. HRTEM image of the film together with the results of FFT are presented in figure 12. These data

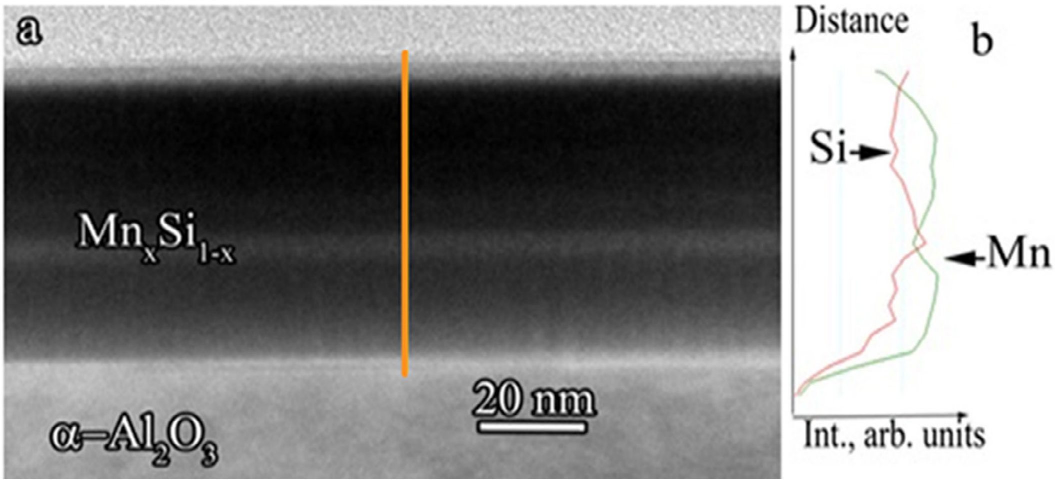

Figure 7. (a) Bright field cross-sectional TEM image of Mn$_x$Si$_{1-x}$film on α-Al$_2$O$_3$ (sample 2) and (b) correspondent EDXS results along the vertical line in figure (a).

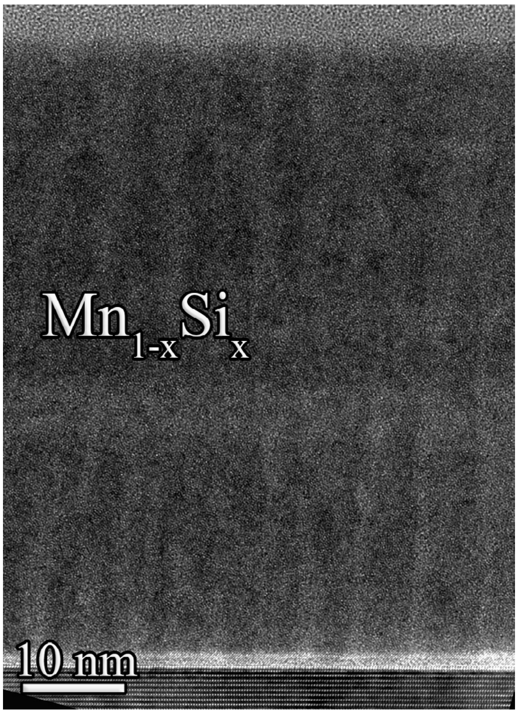

Figure 8. The enlarged Bright field cross-sectional TEM image of Mn$_x$Si$_{1-x}$film on α-Al$_2$O$_3$ (sample #2).

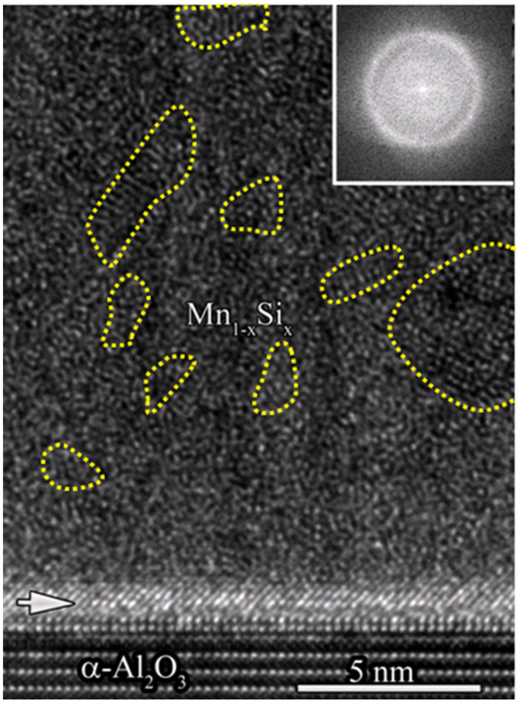

Figure 9. Bright field HRTEM cross-sectional TEM image of Mn$_x$Si$_{1-x}$/α-Al$_2$O$_3$ interface (sample 2). Some of the MnSi B20 nanoccrystallites 2–5 nm in size are shown with dotted circles. FFT spectra from Mn$_x$Si$_{1-x}$ film is shown in the inset.

demonstrate that the film like 'a-type' samples consists of defective B20 MnSi nanocrystallites embedded in amorphous matrix. The morphology of the film is layered and that was observed both in HAADF STEM and in HRTEM images. Samples of 'b-type' compared to 'a-type' exhibited a much higher amount of amorphous fraction, less homogeneity, stronger disorder and smaller density of B20 MnSi.

5. Discussion

From the temperature dependence of the saturation magnetization M_s and the thermoremanence magnetization M_r we can conclude that the samples contain three magnetic phases: the low temperature magnetic phase (1) with Curie temperature ≈ 30 K; the high temperature phase (2) with Curie temperature about 300 K for the samples of the group ('a') and 230 K for the samples of the group ('b'). Third superparamagnetic phase (3) is essential in 'b-type' samples, for 'a-type' samples it is not so efficient. The high temperature phase (2) is of practical importance for spintronics and for the formation of bulk semiconductors with a high Curie temperature compatible with Si microelectronic technology. Based on the structural studies we try to reveal the origin of magnetic moments and the difference between two groups of samples.

TEM and EDS studies demonstrate that the composition of the samples along the thickness changes at the surfaces and interfaces while it slightly varies in the medium part of the

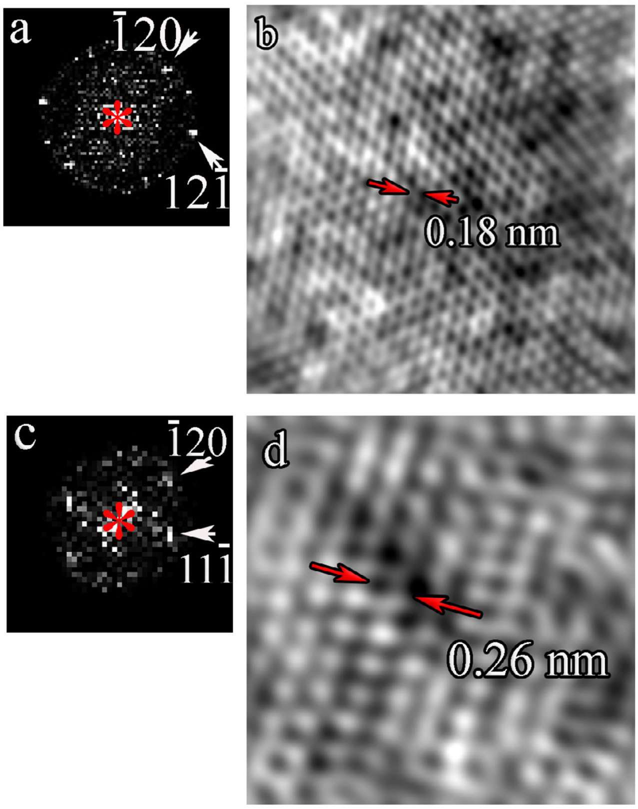

Figure 10. (a) The FFT pattern of MnSi nanocrystallite particle (sample 2), shown in (b) demonstrating B20 crystal structure in $[-2\ -1\ -4]$ zone axis (bright field HRTEM image). (c) The FFT pattern of MnSi particle shown in (d) and obtained in $[-2\ -1\ -3]$ zone axis (sample 2).

sample (see figure 7). We believe that just the medium region being the main volume of the sample (see figure 7(b)) and containing crystallites (crystalline grains, see figure 10 and previous section) contributes most to the high temperature ferromagnetic ordering. These crystallites form the columnar morphology of the film (figure 8). For samples of 'b-type' the columnar film structure is not so pronounced as for the 'a-type' (compare figures 8 and 12). For both types of samples these columns are embedded in the amorphous matrix. The partial volume of amorphous phase is larger in 'b-type' samples, being the reason for smaller values of M_s and M_r in these samples compared with 'a-type' samples.

The mentioned above nanocrystallites have the size of about 2–5 nm (see figure 9) and their crystal structure adopts B20 MnSi crystal type with high density of structural defects. Detected magnetic moments per Mn atom are up to $1.4\mu_B$ and $0.74\mu_B$ for 1 and 3 samples, respectively. However, these values are much higher than in MnSi single crystal in the ferromagnetic state ($\approx 0.4\mu_B$) [21]. As proposed in [19, 34] the high value of the magnetic moments is associated with point magnetic defects arising due to the absence of local ordering in Mn site, related to the lack of the stoichiometry, in particular for $Si_{1-x}Mn_x$ structures such magnetic moments could originate from Si vacancies [34].

TEM studies show that our samples exhibit the columnar morphology (see figures 7–9). The columns contain B20 MnSi nanocrystallites (nanocrystalline particles), some parts of which are marked in figure 9 by dashed circles. Some of them could be responsible for the first, low temperature phase, which is related to MnSi magnetic contribution. However these nanocrystallites mainly are strongly defected. The stoichiometry slightly deviates to a smaller Si concentration, so Si vacancies with strong local magnetic moments are good candidates for the origin of these defects. These defected MnSi nanocrystallines have strong magnetic moments and interact with each other. They form ferromagnetic clusters due to the magnetic interaction between them. They are magnetic clusters but not crystallite clusters formed by magnetic interaction and consist of separated nanocrystallites with uniformly oriented magnetic moments. These clusters could form the ferromagnetic state under external magnetic field or mutual interaction if the corresponding energy overcome the anisotropy one. Therefore the size of these clusters depends on temperature and external magnetic field and is estimated to be in the range of several tens of nm. The size of ferromagnetic clusters increases with applied magnetic field due to the assembling of additional magnetic crystallites to the cluster. The zero field and field cooling (ZFC and FC) curves (see figure 6) give a hint for presence of the magnetic clusters. In the absence of magnetic field or in case of weak interaction between these magnetic clusters ZFC curves exhibit a spin glass behavior [35].

The ferromagnetic state formed by the interaction between these magnetic clusters could be the nature of the second high-temperature phase. The possible cause of the long range high-temperature ferromagnetic ordering in the second magnetic phase is related to the theory developed in [19]. The main idea of this theory is that the high temperature ferromagnetism appears due to the high temperature magnetic moments (in our case magnetic clusters mentioned above) inside a matrix while the exchange between these moments occurs through the magnetic fluctuations (paramagnons). Here it should be mentioned that the RKKY contribution to the ferromagnetic state in $Si_{1-x}Mn_x$ was estimated to be not sufficient for the room value of the Curie temperature. Because this estimation demonstrates that RKKY interaction could be responsible only for the low T_C value, which is not more than 10 K as was discussed in [19]. The paramagnons naturally exist in the weak ferromagnetic host Mn-Si amorphous matrix far above its intrinsic Curie temperature $T_{C1} \approx 30$ K. Originally, such a mechanism was suggested for GaMnAs [36]. This interaction relates to the theory of the Stoner enhancement of the ferromagnetic interaction.

According to small values of $M_{s1}(0)$ and M_3 in the samples 1 and 2 we proposed that phase 2 is dominant for 'a-type' samples. The high temperature ferromagnetic state was not observed in MnSi samples with deviation from the stoichiometry prepared by other methods [6, 27]. It may be a hint that the nature of high temperature ferromagnetism could be related to the film growth technology and to the formation of the magnetic moments, magnetic clusters. The variation of the PLD technique strongly affects the parameters of the high temperature ferromagnetic state [17].

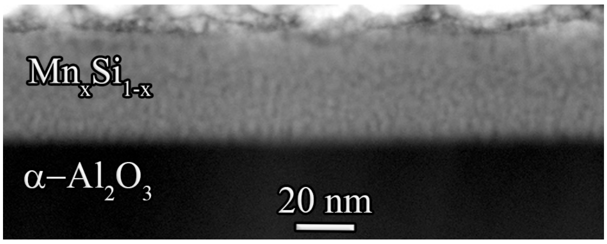

Figure 11. Cross-sectional HAADF STEM image of Mn_xSi_{1-x}film on α-Al_2O_3 (sample 4).

The interaction between magnetic clusters and external magnetic fields causes the formation of the ferromagnetic state. The external magnetic field leads to the polarization of magnetic clusters and therefor enhances the interaction. The interaction makes the ferromagnetic state stable even after switching off the magnetic field and reveals the remanent magnetization and hysteresis behavior as shown in figures 3 and 4.

The formation of the long range ferromagnetic ordering from small magnetic clusters is of the percolation type. It means that only some part of the small magnetic clusters with sizes of several tens of nm formed from magnetic nanocrystallites of 2–5 nm in sizes (figure 9) creates the magnetic moment. Part of these clusters, which are located close to each other and interact strongly enough, is forming the long range ferromagnetic percolation cluster, while other clusters still act as individual superparamagnetic particles giving rise to the superparamagnetic contribution to the magnetic properties of the material. Also there is an amorphous weak helicoidal ferromagnetic Si–Mn fraction acting as a matrix. These different fractions of the sample volume correspond to three different magnetic phases (1, 2, and 3) mentioned above. The volume of each phase depends on the concentration of clusters and the matrix microstructure and thus on the technology parameters. The variation of this volume could be responsible for the difference in $M_{s2}(0)$ value as it was observed in the samples 1 and 3.

The volume of the percolation ferromagnetic cluster increases with magnetic field. This cluster assembles large magnetic clusters, the other one contributes to the supermagnetic volume, which contains smaller magnetic clusters. One could expect that with increasing magnetic field the amount of clusters contributing to the superparamgnetic properties will decrease. ZFC measurements are related to these properties and the temperature of the maximum of M at ZFC curve could be accepted as the blocking temperature—T_b. The external magnetic field enhances the interaction between small magnetic clusters and leads to the increase of their size. That is why the blocking temperature changes strongly with a magnetic field (see figure 6).

Now let us discuss the reason for the difference of T_{C2} values for two types of samples presented in figures 2(a) and (b). The most probable reasons are variations of the magnetic crystallites concentration as well as the volume and composition of the amorphous matrix, in which magnetic clusters formed of the above-mentioned magnetic crystallites are embedded. Both of these reasons are responsible for the strength of the exchange interaction. This assumption is proved by the comparison of figures 8 and 11. The fraction of crystalline nanoparticals in the 'b-type' samples is lower than in 'a-type' ones. As a result, the $M_{s2}(0)$ values for the samples 2 and 4 are different. It is seen that the partial volume filled by columns is much larger while the volume of amorphous phase is much smaller in the sample of the group 'a' than in the sample from the group 'b'.

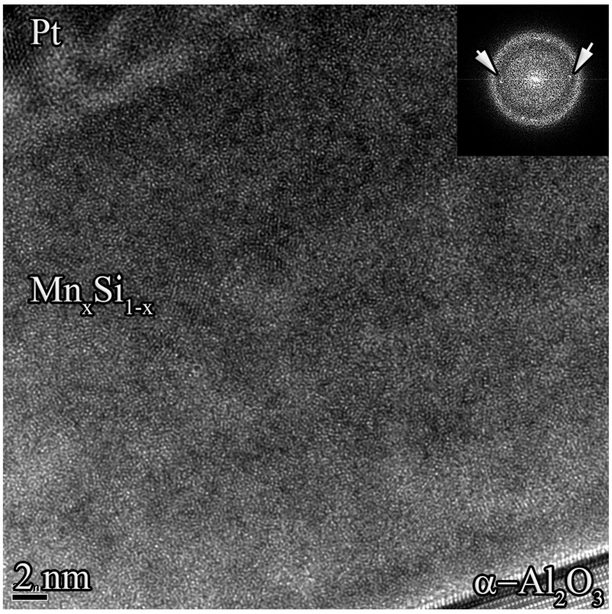

Figure 12. Bright field HRTEM cross-sectional TEM image of Mn_xSi_{1-x}/α-Al_2O_3 interface (sample 4). The FFT power spectra from the film area is in the inset. The circle on the FFT pattern corresponds to 0.21 nm (reflections from (2 1 0) and (1 2 0) crystal planes). The reflections marked by arrows corresponded to 111 reflection.

Proposed model reveals the nature of the high temperature ferromagnetic state (phase 2) as well as explains the reason for the formation of low temperature (phase 1) and superparamagnetic phases. Phase 1 corresponds to amorphous Mn–Si, while the paramagnetic phase could be composed from above mentioned magnetic clusters located far from each other, weakly interacting and behaving as individual superparamagnetic particles.

6. Conclusions

In this paper we present a detailed study of magnetic properties accompanied by SEM/TEM analysis of the structure with atomic size resolution of high temperature ferromagnetic semiconductor $Si_{1-x}Mn_x$ ($x \approx 0.5$) with a small deviation from the stoichiometry $\Delta x < 0.1$. It is shown that the high-temperature ferromagnetic phase arises due to the magnetic crystallites embedded in amorphous matrix of manganese silicide. The crystal structure of crystallites is of B20 MnSi type with a high density of structural defects, mainly Si-vacancies and the absence of local ordering in Mn site, which according to [34] possess magnetic moment. The crystallites form magnetic clusters and the exchange between them occurs by magnetic fluctuation (paramagnons) and leads to the formation of long range ferromagnetic ordering.

The main result of this paper is: we revealed the microstructural reason for the above room temperature ferromagnetic state in the MnSi structures with small deviation from the stoichiometry, which could be interesting for the spintronic applications and presented a detailed description of such material grown by the droplet free PLD technique.

Acknowledgments

ABA and VAL were partly supported by Indian – Russian DST-MSE 14.613.21.0019 -RFMEFI61314X0019. ABA is grateful to Semisalova AS for the help in measurements. DAB was partly supported by RFBR grant № 15-07-06081. The work was supported in part of equipment by M.V.Lomonosov Moscow State University Program of Development.

References

[1] Fabian Z J and Spintronics D S 2004 Fundamentals and applications *Rev. Mod. Phys.* **76** 323

[2] Jungwirth T, Sinova J, Măsek J, Kŭcera J and MacDonald A H 2006 Theory of ferromagnetic (III,Mn)V semiconductors *Rev. Mod. Phys.* **78** 809

[3] Dietl T 2007 *Lecture Notes on Semiconductor Spintronics* (Berlin: Springer)

[4] Panguluri R P, Ku K C, Wojtowicz T, Liu X, Furdyna J K, Lyanda-Geller Y B, Samarth N and Nadgorny B 2005 Andreev reflection and pair-breaking effects at the superconductor/magnetic semiconductor interface *Phys. Rev.* B **72** 054510

[5] Wang M, Marshall R A, Edmonds K W, Rushforth A W and Campion R P 2014 Determining Curie temperatures in dilute ferromagnetic semiconductors: high Curie temperature (Ga, Mn) As *Appl. Phys. Lett.* **104** 132406

[6] Zhou S and Schmidt H 2010 Mn-doped Ge and Si: a review of the experimental status *Materials* **3** 5054

[7] Bolduc M, Awo-Affouda C, Stollenwerk A, Huang M B, Ramos F G, Agnello G, and LaBella V P 2005 Above room temperature ferromagnetism in Mn-ion implanted Si *Phys. Rev.* B **71** 033302

[8] Dubroca T, Hack J, Hummel R E and Angerhofer A 2006 Quasiferromagnetism in semiconductors *Appl. Phys. Lett.* **88** 182504

[9] Orlov A F *et al* 2009 Structure, electrical and magnetic properties, and the origin of the room temperature ferromagnetism in Mn-implanted Si *JETP* **109** 602

[10] Zhou S *et al* 2007 Structural and magnetic properties of Mn-implanted Si *Phys. Rev.* B **75** 085203

[11] Zeng L, Helgren E, Rahimi M, Hellman F, Islam R, Wilkens B J, Culbertson R J and Smith D J 2008 Quenched magnetic moment in Mn-doped amorphous Si films *Phys. Rev.* B **77** 073306

[12] Awo-Affouda C, Bolduc M, Huang M B, Ramos F G, Dunn K A, Thiel B, Agnello G and LaBella V P 2006 Observation of crystallite formation in ferromagnetic Mn-implanted Si *J. Vac. Sci. Technol.* A **24** 1644

[13] Zhou S, Shalimov A, Potzger K, Helm M, Fassbender J and Schmidt H 2009 $\mathrm{MnSi}_{1.7}$ nanoparticles embedded in Si: superparamagnetism with collective behavior *Phys. Rev.* B **80** 174423

[14] Aronzon B A *et al* 2011 Room-temperature ferromagnetism and anomalous Hall effect in Si_{1-x} Mn_x ($x \approx 0.35$) alloys *Phys. Rev.* B **84** 075209

[15] Nikolaev S N *et al* 2012 High temperature ferromagnetism of Si_{1-x} Mn_x films fabricated by laser deposition using the droplet velocity separation technique *Semiconductors* **46** 1510

[16] Rylkov V V *et al* 2012 High-temperature ferromagnetism in Si_{1-x} Mn_x ($x \approx 0.5$) nonstoichiometric alloys *JETP Lett.* **96** 255

[17] Nikolaev S N 2016 Ferromagnetism of $\mathrm{Mn}_x\mathrm{Si}_{1-x}$($x$ ~ 0.5) films grown in the shadow geometry by pulsed laser deposition method *AIP Adv.* **6** 015020

[18] Khaydukov E V, Novodvorsky O A, Rocheva V V, Lotin A A, Zuev D A and Khramova O D 2011 Ion energy spectrum control in modified cross-beam pulsed laser deposition method *Tech. Phys. Lett.* **37** 69

[19] Men'shov V N, Tugushev V V, Caprara S and Chulkov E V 2011 High-temperature ferromagnetism in Si:Mn alloys *Phys. Rev.* B **83** 035201

[20] Gottlieb U, Sulpice A, Lambert-Andron B and Laborde O 2003 Magnetic properties of single crystalline $\mathrm{Mn}_4\mathrm{Si}_7$ *Alloys Comp.* **361** 13
Sulpice A, Gottlieb U, Affronte M and Laborde O 2004 Magnetic and electronic properties of MnSi *J. Magn. Magn. Mater.* **272–6** 519

[21] Stishov S M and Petrova A E 2011 Itinerant helimagnet MnSi *Phys.—Usp.* **54** 1117

[22] Demishev S V 2012 Magnetic phase diagram of MnSi in the high-field region. *Phys. Rev.* B **85** 045131

[23] Glushkov V V, Lobanova I I, Ivanov V Yu, Sluchanko N E and Demishev S V 2015 Anomalous Hall effect in MnSi: intrinsic to extrinsic crossover *JETP Lett.* **101** 459

[24] Jeong T and Pickett W E 2004 Implications of the B20 crystal structure for the magnetoelectronic structure of MnSi *Phys. Rev.* B **70** 075114

[25] Dmitriev V, Chernyshov D, Grigoriev S and Dyadkin V 2012 A chiral link between structure and magnetism in MnSi *J. Phys.: Condens. Matter* **24** 366005

[26] Higashi S, Kocan P and Tochihara H 2009 Reactive epitaxial growth of MnSi ultrathin films on Si(1 1 1) by Mn deposition *Phys. Rev.* B **79** 205312

[27] Yang A-C *et al* 2015 Superparamagnetism, magnetoresistance and anomalous Hall effect in amorphous Mn_xSi 1À$_x$ semiconductor films *J. Alloys Compd.* **623** 438

[28] Lotin A A, Novodvorsky O A, Khaydukov E V, Rocheva V V, Khramova O D, Panchenko V Ya, Wenzel C, Trumpaicka N and Shcherbachev K D 2010 Epitaxial growth and properties of $\mathrm{Mg}_x\mathrm{Zn}_{1-x}\mathrm{O}$ films produced by pulsed laser deposition *Semiconductors* **44** 246

[29] Aronzon B A, Meilikhov E Z and Lazarev S D 1995 *Handbook of Physical Quantities* ed I S Grigoriev and E Z Meilikhov (Boca Raton, FL: CRC Press)

[30] Stadelmann P A 1987 EMS—a software package for electron diffraction analysis and HREM image simulation in materials science *Ultramicrocopy* **21** 131

[31] Moca C P, Sheu B L, Samarth N, Schiffer P, Janko B and Zarand G 2009 Scaling theory of magnetoresistance and carrier localization in Ga_{1-x} $\mathrm{Mn}_x\mathrm{As}$ *Phys. Rev. Lett.* **102** 137203

[32] Aindow M 1990 Interfacial structure in heteroepitaxial silicon on sapphire *J. Am. Ceram. Soc.* **73** 1136

[33] Jorgensen J-E and Rasmussen S E 1991 Refinement of the structure of MnSi by powder diffraction *Powder Diff.* **6** 194

[34] Caprara S, Kulatov E and Tugushev V.V 2012 Half-metallic spin polarized electron states in the chimney-ladder higher manganese silicides MnSi_{1-x} ($x = 1.75 - 1.73$) with silicon vacancies *Eur. Phys. J.* B **85** 149

[35] Chowdhury D 1986 *Spin Glasses and Other Frustrated Systems* (Singapore: World Scientific)

[36] Jungwirth T *et al* 2005 Prospects for high temperature ferromagnetism in (Ga,Mn)As semiconductor *Phys. Rev.* B **72** 165204